Materials & Design 231 (2023) 112031

Contents lists available at ScienceDirect

Materials & Design

journal homepage: www.elsevier.com/locate/matdes

In situ X-ray imaging of hot cracking and porosity during LPBF of Al-2139 with TiB_2 additions and varied process parameters

David T. Rees [a,b,*], Chu Lun Alex Leung [a,b,*], Joe Elambasseril [c], Sebastian Marussi [a,b], Saurabh Shah [a,b], Shashidhara Marathe [d], Milan Brandt [c], Mark Easton [c], Peter D. Lee [a,b,*]

[a] UCL Mechanical Engineering, University College London, WC1E 7JE, UK
[b] Research Complex at Harwell, Harwell Campus, Didcot OX11 0FA, UK
[c] Centre for Additive Manufacturing, RMIT University, PO Box 2476, Melbourne, VIC 3001, Australia
[d] Diamond Light Source Ltd, Harwell Campus, Didcot OX11 0DE, UK

HIGHLIGHTS

- The addition of TiB_2 suppresses hot crack formation during LPBF of Al-2139.
- TiB_2 reduces the volume fraction, length, breadth, and surface area of hot cracks.
- Porosity is increased by the addition of TiB_2, especially at high energy densities.

GRAPHICAL ABSTRACT

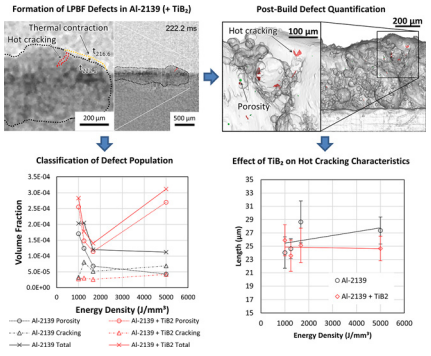

ARTICLE INFO

Article history:
Received 27 January 2023
Revised 18 May 2023
Accepted 22 May 2023
Available online 6 June 2023

Keywords:
Additive manufacturing
Laser powder bed fusion
Aluminium alloys
X-ray imaging
Hot cracking

ABSTRACT

Laser powder bed fusion (LPBF) additive manufacturing of 2XXX series Al alloys could be used for low volume specialist aerospace components, however, such alloys exhibit hot cracking susceptibility that can lead to component failure. In this study, we show two approaches to suppress the formation of hot cracks by controlling solidification behaviour using: (1) TiB_2 additions; and (2) optimisation of LPBF process parameters. Using high-speed synchrotron X-ray radiography, we monitored LPBF of Al-2139 *in situ*, with and without TiB_2 under a range of process conditions. *In situ* X-ray radiography results captured the crack growth over 1.0 ms at a rate of *ca.* 110 mm s^{-1}, as well as pore evolution, wetting behaviour and build height. High-resolution synchrotron X-ray computed tomography (sCT) was used to measure the volume fraction of defects, *e.g.* hydrogen pores and microcracks, in the as-built LPBF samples. Our results show adding TiB_2 in Al-2139 reduces the volume of cracks by up to 79 % under a volume energy density of 1000 to 5000 J mm^{-3}, as well as reducing the average length, breadth, and surface area of cracks.

1. Introduction

Laser additive manufacturing (LAM) processes involve the fusion of powder materials by the controlled scanning of a focused laser beam over subsequent layers to produce complex 3D

* Corresponding authors at: Department of Mechanical Engineering, University College London, WC1E 7JE, UK.
E-mail addresses: david.rees.14@ucl.ac.uk (D.T. Rees), alex.leung@ucl.ac.uk (C.L.A. Leung), peter.lee@ucl.ac.uk (P.D. Lee).

https://doi.org/10.1016/j.matdes.2023.112031
0264-1275/

components. In the case of laser powder bed fusion (LPBF), the laser achieves full or partial localised melting of a powder bed. The bed is then lowered, and a new layer of powder is spread, with the process repeating until a complete part is built [1]. LPBF is of increasing interest for aerospace applications due to the inherent advantages over traditional methods, including increased geometric design freedom and the rapid transition of 3D digital designs into final components [2].

2xxx series aluminium (Al) alloys are employed in aerospace applications because of their excellent specific strength, thermal and electrical conductivity, and corrosion resistance [3]. Mechanical working is typically required to achieve peak strength through homogeneous nucleation of a precipitating phase, however precipitates uniformly nucleate in Al-2139 through rapid cooling [4]. Since a mechanical working process step would oppose some of the advantages of LAM, Al-2139 is more suitable for additive manufacturing (AM) processes than Al alloys requiring work hardening. A drawback of using Al-2139 is its hot cracking susceptibility, which leads to sub-optimal bulk mechanical performance [5–7]. Al-2139 is used in a broad range of aerospace applications [8] where components experience cyclical loading, and could, therefore, fail by fatigue due to the presence of hot cracks. To facilitate the adoption of LPBF components in these applications, new strategies are needed to mitigate the formation of defects and quantify them in relation to fatigue life.

A variety of features detrimental to mechanical performance have been observed in as-built LAM components, such as surface roughness [9], undesirable metallurgical features, microstructural inhomogeneity [10–12] and residual stresses [1,13]. The most detrimental of these build features are defects [14], *e.g.* lack of fusion (LoF) [15] and porosity [16]. LoF forms due to insufficient powder melting whereas porosity is caused by: trapped gas in the feedstock material [17]; decomposition of oxides [18,19]; gas desorption [20]; selective evaporation of light elements [21,22]; and keyhole instability [23]. Pores act as local stress concentrators and initiation sites for fatigue cracks, reducing global yield strength and fatigue resistance. However, pre-existing cracks introduced during fabrication are even more severe due to their greater length and higher aspect ratio.

Several mechanisms can cause cracking during LPBF [24]. Cracking can occur during the solidification or liquation of certain alloy systems, known as hot cracking or hot tearing. These cracking mechanisms have been observed in aluminium alloys [25,26], nickel alloys [27,28], and steels [29]. Hot cracking is driven by residual stresses induced during solidification. When there is a difference between the freezing point of the bulk phase(s) and low freezing point eutectics, liquid films form at inter-dendritic boundaries [30]. As the solidified metal cools and contracts the interfacial tension can tear the eutectic liquid film, which becomes the initiation site for a hot crack. This mechanism acts similarly for many alloy systems in which hot cracking occurs. However, the elements that constitute the eutectic phase can be introduced from varying sources [31]. In the case of Al alloys, the alloying elements form a range of eutectics (α + Si in Al-Si systems, and α + θ in Al-Cu systems). Therefore, some Al alloys are susceptible to this cracking mechanism and highly sensitive to changes in alloy composition [32].

Hot cracking can easily occur during LAM, analogous to hot cracking in high speed welding with continuous wave lasers [33]. The propensity for hot cracking can be attributed to microsegregation resulting from highly non-equilibrium cooling at the order of 10^5 K s^{-1} [34] and solidification at rates of 0.1 to 5 m s^{-1} [12]. These conditions result in aligned columnar grain structures with grain boundaries that cracks can propagate along more easily than in equiaxed microstructures [35]. Additionally, the high temperature gradients result in large residual strains that can drive hot cracking. Insufficient liquid feeding is another important factor in determining hot cracking susceptibility [25]. With the high thermal gradients of laser melting, the rate of shrinkage of the solid phase may be greater than the rate of liquid feeding in the inter-dendritic region [36], which would result in cracking during solidification. The challenges of LAM identified here, along with the inherent susceptibility of some Al alloys to hot cracking, emphasise the need for suitable strategies to mitigate or eliminate hot cracking in these alloys if components made from them are to be used in service.

A common strategy in AM to improve part density and eliminate defects is the optimisation of process parameters. Stopyra *et al.* [37] used this strategy to try and achieve defect-free components of AA7075. They found that by performing multi-stage optimisation, from single tracks to thin walls and volumetric specimens, they could achieve a part density above 99 % and reduced vapour losses of alloying elements. However, they reported that solidification cracks could not be eliminated.

In welding, it has been shown that reducing the grain size in the weld metal can suppress hot cracking [32]. This can be achieved by the addition of grain refiners that reduce the critical amount of undercooling needed to facilitate equiaxed grain growth [38]. Martin *et al.* [12] demonstrate one way to control solidification in LPBF of aluminium alloys by promoting nucleation of new grains with hydrogen-stabilised zirconium nucleants assembled on Al-7075 alloy powder feedstock particles. They reported achieving crack-free builds with small equiaxed grains and higher strengths than conventional Al alloys produced using AM, but did not investigate the crack formation mechanism, or provide 3D quantification of crack density or morphology. Ho *et al.* [39] studied the effect of eutectic WC-W_2C phase inoculant powders on the microstructural evolution of IN718 during LPBF. Grains smaller than those in the bulk of the as-built sample were observed nucleated on the surface of inoculant particles. However, a recrystallised region of significant size was only achieved by post heat treatment, and the influence of inoculants on the formation of porosity or cracking was not investigated. Elambasseril *et al.* [40] studied the effect of grain refinement on the hot tearing susceptibility of Al-2139 in LPBF and found that TiB_2 additions showed a clear effect in eliminating hot tearing for energy densities below 2000 J mm^{-3}. However, this study did not observe the effect via *in situ* experiments, or provide 3D quantification of crack density or morphology, so it is still unclear whether hot tearing was eliminated. In addition, the hot cracking susceptibility at energy densities greater than 2000 J mm^{-3} was not explored.

Grain size can also be controlled in AM by altering the scan speed of the laser beam. Increasing scan speed causes average grain size to lower [40,41], but promotes higher temperature gradients and epitaxial columnar grain growth [42] resulting in a strong texture and which could increase hot cracking susceptibility. The laser scanning pattern used can also lead to substantial changes in the resultant microstructure, such as a strong fibrous texture being altered into a weak cube texture solely by a rotation of the scanning vectors [43].

There are many areas that need to be explored further when it comes to hot cracking in AM. Many studies rely on scanning electron microscope (SEM) images for quantifying cracks in 2D, however, SEM does not provide 3D quantification of the crack geometry, surface area, or volume fraction, which is needed for modelling these microstructural features and ultimately certifying AM parts for use in-service. There is a lack of data available showing crack formation as it occurs. To date, hot cracking during AM has not been widely investigated using *in situ* or X-ray imaging techniques [44,45]. The majority of *in situ* synchrotron studies have focused on melt pool behaviour and pore formation in single-layer builds [18,19,21,46]. If these techniques can be applied to the

problem of hot cracking in AM of multi-layer builds understanding of the phenomena will be improved and enable more accurate modelling of the process, and the development of crack mitigation/elimination strategies for AM.

Our objectives for this study are to observe hot cracking of Al-2139 by *in situ* synchrotron X-ray imaging to investigate the effect of TiB_2 additions and parameters with energy densities ranging from 1000 to 5000 J mm^{-3}, and perform 3D quantification of cracks and pores. We capture the rapid dynamics of hot crack formation during multilayer LPBF of Al-2139. Post-build, we use synchrotron X-ray computed tomography to quantify the influence of TiB_2 additions and process parameters, as well as electron microscopy and energy dispersive spectroscopy to inspect build quality.

2. Materials and methods

2.1. In situ and operando synchrotron X-ray radiography

Gas atomised Al-2139 powder and an Al-2139 powder prealloyed with Al-5Ti-1B to form TiB_2 grain refiners (0.2 wt% Ti and 0.03 wt% B [40]) were selected for this study, both provided by ECKA Granules Germany GmbH. Both materials were processed using a powder layer thickness of 40 μm, building 15 layers on top of an Al substrate of 99 % purity, temper: half hard (Goodfellows, UK) in an area of 45 × 0.3 mm^2. The laser beam (wavelength 1030–1070 nm) was scanned across a 5 mm line along the powder bed with the maximum power of 200 W in an argon atmosphere at a flow rate of 4 l min^{-1}. The scan direction was reversed with each consecutive layer for a bi-directional build strategy [47]. The scan velocity used for each build is shown in Table 1. Lower laser powers were not considered due to the high reflectivity of the material [48] (shown in **Supplementary** Fig. 2). The volume energy density, *VED*, was calculated for each build using equation (1) for focused beam diameter [49]:

$$VED = \frac{P}{v \cdot d \cdot t} \quad (1)$$

where P is laser power, v is scan speed, d is beam diameter, and t is layer thickness.

To observe the laser-matter interaction and formation of hot cracks, we performed LPBF experiments with both powder types using our *In Situ* and *Operando* powder bed Process Replicator (ISOPR) [46]. An imaging setup on the I13-2 beamline at Diamond Light Source (DLS), UK [50] was used to collect *in situ* radiographs that captured the process. A 25 keV X-ray beam passed through the ISOPR perpendicular to the laser scan direction and parallel to the substrate top surface, generating a side-view of the process. A Photron FASTCAM SAZ 2100 K CCD detector was used with an acquisition rate of 5000 fps. The sensor provided a field of view (FOV) of 5.1 × 5.1 mm, comprised of 1024 × 1024 pixels for an effective pixel size of 4.98 μm (see [22] for details).

The process parameters shown in Table 1 were selected with the limitations of the described imaging system and the ISOPR in mind, while best accounting for the high-power-high speed conditions preferred by manufacturers. An initial scan speed of 25 mm s^{-1} was selected as a starting point for the *in situ* study to investigate what phenomena could be captured in the radiography. The results of the 25 mm s^{-1} build have been included in §3.1 as they exemplify the types of features present. After performing this experiment, we conducted process mapping to explore the effect of varying scan speed on the hot cracking susceptibility of Al-2139. Scan speeds slower than industrial conditions result in features of sufficient size for *in situ* observations to be made, which are used alongside post-build characterisation to infer how hot cracking and other build features form at higher scan speeds.

2.2. Synchrotron X-ray computed tomography

The as-built samples were scanned using synchrotron X-ray computed tomography (sCT) to characterise the volume fraction of cracks and pores, as well as their size distribution and morphology in three dimensions. These scans were conducted at the I13-2 beamline at DLS, UK. A pink X-ray beam, with high and low bandwidth filters, centred around 27 keV was passed through the as-built samples. A 2560 × 2160 CMOS sensor (pco.edge 5.5 camera, PCO AG, Kelheim, Germany) with a 4x objective lens coupled to a 100 μm thick LuAG:Ce scintillator was used to record the projection images. For each scan 2500 projection images were recorded over a 180° rotation of the sample about the longitudinal axis with an exposure time of 0.150 s for each image. The 2.1 × 1.8 mm FOV gave an effective pixel size of 0.8125 μm and was centred on the middle of the track along the longitudinal axis to inspect a steady-state region of the melt track. The through-thickness slices were reconstructed using Savu (Data Analysis group DLS, UK) [51].

The use of sCT was necessary for quantifying the defect population in each sample as we expected the majority of features to be on the micro-scale and not quantifiable in the *in situ* radiography due to the limited spatial resolution and inherent noise. The sCT set-up used provides a resolution one order of magnitude smaller than our radiography imaging set-up, enabling micro-scale defects to be captured and quantified. Therefore, we expected to see a greater number of defects using this technique compared to our *in situ* radiography results.

2.3. SEM and EDS analysis

The surface waviness of the as-built samples was evaluated using SEM (SEM, JEOL JSM-6610LV, Japan). We imaged the top and side views of each specimen in a FOV of 1830 × 1245 μm at 70x magnification. A series of secondary electron images were taken across the length of the track with a step size of 750 μm, and combined to produce a single image using the Pairwise stitching plugin from ImageJ [52]. The stitched side views of each track were segmented to produce binary masks. These masks were

Table 1
Process parameters selected for this study.

Sample ID	Material	Laser power, P [W]	Scan speed, v [mm s^1]	Layer thickness, t [μm]	Beam diameter, f [μm]	Volume Energy Density, *VED* [J mm^3]
S1	Al-2139	200	25	40	50	4000
S2	Al-2139	200	20	40	50	5000
S3	Al-2139	200	60	40	50	1667
S4	Al-2139	200	80	40	50	1250
S5	Al-2139	200	100	40	50	1000
S6	Al-2139 + TiB_2	200	20	40	50	5000
S7	Al-2139 + TiB_2	200	60	40	50	1667
S8	Al-2139 + TiB_2	200	80	40	50	1250
S9	Al-2139 + TiB_2	200	100	40	50	1000

imported into MATLAB 2019a to generate a contour plot of the top surface, which was used to quantify the surface waviness.

The chemical composition of the melt track surface and cross-section were characterised using energy dispersive X-ray spectroscopy (EDS) with an X-Max 80 mm^2 EDS-detector. Samples were prepared by sectioning perpendicular to the laser scanning direction 2.5 mm from the end of the track before being ground and polished to a 0.04 μm finish.

2.4. Image processing and quantification

The radiographs were processed using a flat field correction and the VBM3D denoising algorithm [53] in MATLAB 2019a, similar to that in [46], to improve the signal to noise ratio, followed by background subtraction to emphasise the melt track, melt pool, cracks and pores.

Pore and crack size distributions for each sample were quantified from the sCT data using Avizo 2019.1 (Thermo Fisher Scientific, US). A mask was generated by passing the images through a kernel of 10 × 10 × 10 Gaussian filter, followed by applying the "Thresholding", "Fill Holes" and "Dilation" AVIZO modules. The mask was applied to remove ring and streak artefacts introduced during reconstruction. The images were then passed through a kernel of 5 × 5 × 5 median filter to remove noise within the sample. The Al-2139 (+TiB_2) phase was segmented from the filtered image by thresholding.

The population of enclosed cracks and pores was segmented by applying the "Fill Holes" Avizo module on the segmented melt track, and then subtracting from the original binary image volume. Connected component analysis of the enclosed features comprised of ≥ 10 voxels was then performed to obtain their volume and surface area (see [54] for similar analysis). The relative density of the parts was calculated by first dividing the volume of cracks and pores by the total volume of the melt track plus cracks and pores, and then subtracting this value from 1. Additional quantification was conducted to determine the volume equivalent diameter and sphericity. According to ref. [15,55], enclosed features with a sphericity of < 0.7 were classified as cracks while those ≥ 0.7 were classified as pores. The sCT analysis excludes defects open to the sample surface such as open pores, open cracks, and LoF as surface defects are likely to be removed by hatching in non-single line scan builds [40].

3. Results and discussion

3.1. LPBF of Al-2139 and Al-2139 + TiB_2 powder

Time-series radiographs of the third layer during an Al-2139 build (sample S1) are shown in Fig. 1 and **Supplementary Video 1**. Melting of the powder is observed at $t_{26.8}$ (Fig. 1**b**). A spherical molten pool forms beneath the laser beam, indicating that the liquid has not wetted the previous layer. Without substantial remelting of the previous layer or wetting, the molten mass retains its spherical shape as it solidifies and is pushed by the flowing atmosphere to rest on the side of the track as a large satellite particle. Several of these large satellite particles can be seen on the final build for both materials across the entire process parameter range, as shown in later sections.

Over the initial few millimetres from the start point, the laser beam strikes the powder, and it melts, but only a discontinuous track is formed. The laser beam causes vaporisation at the surface of the molten pool, generating a recoil pressure and resulting in a vapour jet, as described by Leung *et al.* [46]. Powder particles are entrainment by this jet and ejected away from the substrate along with some molten spatter [56]. From $t_{103.8}$ to $t_{114.0}$, powder in the regions along the scan line between the discontinuous parts of the melt track is sintered and pulled up onto the track's top surface (Fig. 1**c**). This phenomenon was observed at scan speeds of 20 and 25 mm s^{-1} during the initial five layers when processing the Al-2139 powder.

A steady state build was reached at $t_{114.0}$. The height of the fused material in the steady state region is 93 ± 13 μm, measured from the top of the previous layer at the same point along the longitudinal axis. The liquid–solid interface of the melt pool and the substrate can now be seen (Fig. 1**c**). As the laser beam passed over a pore in the built track from $t_{140.0}$ to $t_{159.8}$, a pore is engulfed by the melt pool and transported via Marangoni flow to the trailing edge [57], where it is locked in place by the solidification front [23].

At the end of the melt track, the height of the fused material increases to ~ 200 μm. We hypothesise that this is due to the bi-directional scan strategy in tandem with the difficulty building at the beginning of the previous layer creating a greater local powder layer thickness, as shown by Sinclair *et al* [55]. A greater volume of powder is deposited on top of the previous layer in this region, which is entrained into the melt pool. After the laser turns off the end of the melt track shrinks in height as the material solidifies. At $t_{216.6}$ the end of the melt track is still above the solidus temperature and a crack starts to form in the mushy zone (Fig. 1**e**). The crack propagates through the build at a 56° angle to the scan direction until it reaches a maximum length of 106 μm at $t_{218.0}$ (Fig. 1**f**), which gives an average growth rate of 76 mm s^{-1}. The crack appears in the radiograph with a higher greyscale value than the surrounding materials. The crack angle and crack length suggest that the crack has propagated normal to the solidification front, through the liquid film between two columnar grains. The grain sizes and grain boundary angles shown in the EBSD results of Elambasseril *et al.* [40] support this inference.

We hypothesise that gas pores trapped by the solidification front can act as initiation sites for hot cracking, as shown in welding [58]. As columnar dendrites grow through the melt pool, pores are captured by secondary dendrite arms and are prevented from moving within the remaining liquid. The pores are then compressed during growth of adjacent grains and take on a morphology with a higher aspect ratio. These sharp discontinuities in the interdendritic regions are ideally placed for hot cracks to propagate from when the neighbouring solid material cools and contracts, and may inhibit liquid feeding.

Fig. 2 and **Supplementary Videos 2 – 3** show time-series radiographs comparing the evolution of defects during the fifth layer of an Al-2139 build (sample S2) and an Al-2139 + TiB_2 build (sample S6) with the same process parameters. In the Al-2139 build, melting has occurred, and a continuous track starts to form by at $t_{13.4}$ (Fig. 2**a**). Balling was not seen in Fig. 1**b**, because the liquid metal has wetted the surface of the previously fused layer due to the slower scan speed. However, humping of the top surface of the melt track can be seen and the amplitude of surface waviness is greater than that of the previously fused layer.

The melt track continues to form as the laser moves across the powder bed, with no discontinuities. At $t_{75.6}$ (Fig. 2**b**) a spherical pore rapidly grows in the wake of the laser beam to a diameter of *ca.* 65 μm. Subsequently, we see the ejection of molten spatter similar to the spatter behaviour seen in layer 3 of sample S1. After laser processing has finished for layer 5, we see places along the melt track where these ejections of molten spatter have landed on the newly fused material, appearing as hemispherical humps on the top surface of the track with a diameter of *ca.* 90 μm.

As the laser approaches the end of the scan line we do not see a significant increase in the height of the fused material as we did in sample S1 layer 3. Sufficient wetting of the previous layer at both ends of the melt track means that a greater local powder layer thickness has not been deposited, and therefore no additional pow-

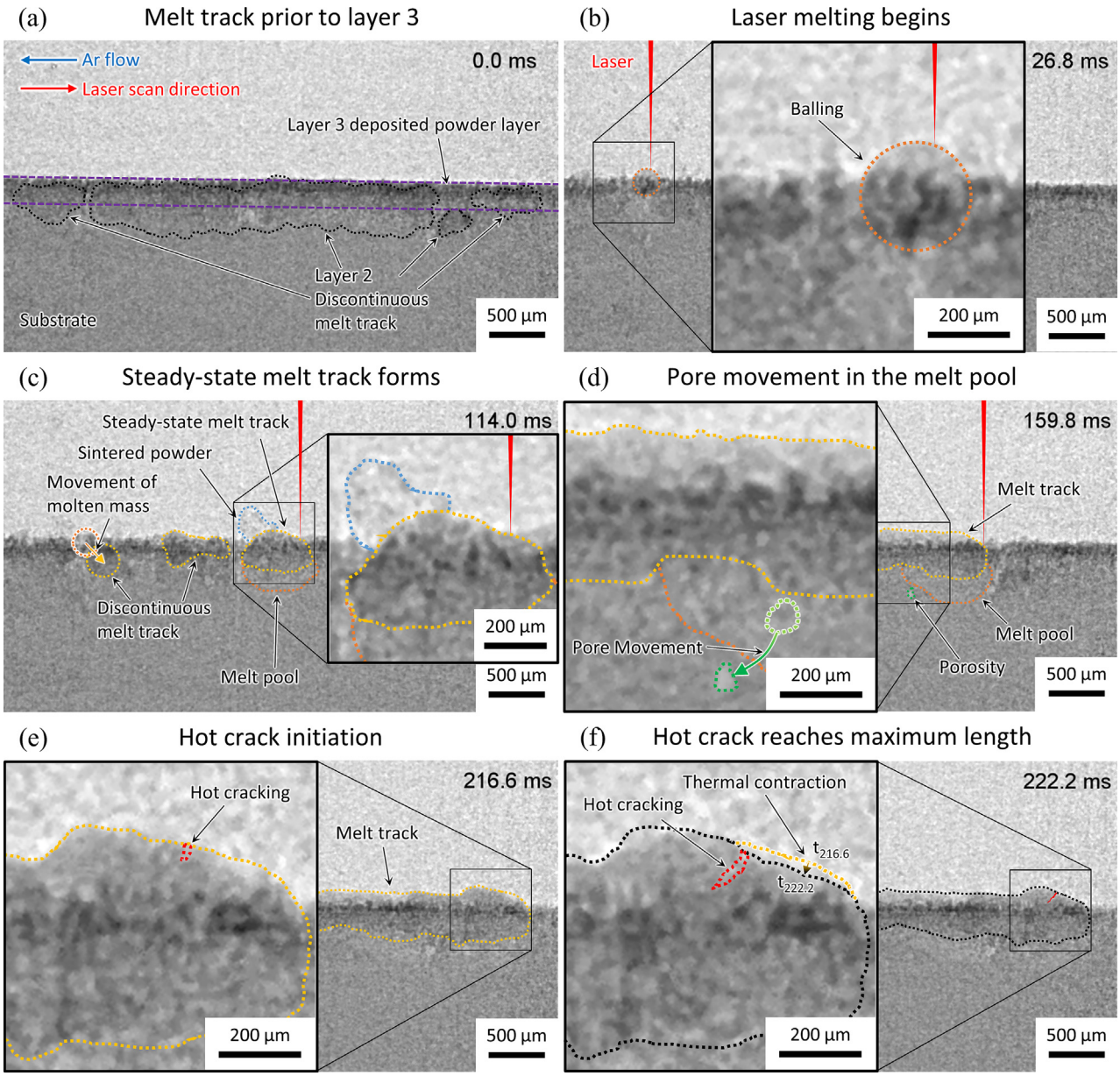

Fig. 1. Time-series radiographs showing hot cracking during Al-2139 LPBF (sample S1 layer 3). Insets show a zoom-in of the key features in each frame. (a) Melt track prior to laser melting (black outline) with deposited powder (purple outline). Direction of the laser beam (red arrow) and gas flow (blue arrow) are shown. (b) Laser melting begins, showing balling of the molten mass (orange outline). The vertical red line shows the approximate position of the laser beam. (c) A steady-state melt track forms (yellow outline) ahead of discontinuous parts of the track (yellow outline). Movement of molten mass before solidification is shown by the yellow arrow and orange outline. Powder is sintered to the top surface of the track (blue outline). The dotted orange line highlights the melt pool boundary. (d) Pore (green outline) movement occurs in the melt pool, shown by the green arrow and dotted light green outline. (e) Initiation of a hot crack (red outline) occurs after the laser is turned off. (f) The hot crack reaches maximum length. Thermal contraction of the melt track is highlighted by the dotted yellow line and arrow, with timestamps labelled. (For interpretation of the references to colour in this figure legend, the reader is referred to the web version of this article.)

der is entrained into the molten pool. At $t_{192.8}$ a crack starts to form in the newly deposited material, terminating at $t_{193.8}$ after growing to 110 µm in length, as seen in Fig. 2**c**. The crack propagates at an angle of 47° to the scan direction, at an average rate of *ca.* 110 mm s^{-1}, and ends at the interface between layers 4 and 5. The crack growth is constrained by the length of the liquid film between grains, as well as the change in grain orientation in the material fused in the fourth layer, which results from the bi-directional scan strategy. The crack evolution observed in layer 5 of sample S2 is of the same nature as the crack evolution seen in layer 3 of sample S1, both of which occurred in the non-grain refined (non-GR) material.

In the Al-2139 + TiB_2 build, melting of the powder was observed at $t_{5.2}$ but a continuous melt track was not formed (Fig. 2**d**). The quantity of powder initially melted was less than in the Al-2139 build, as shown by the height of fused material at the beginning of the fifth layer and from previous layers, possibly due to lower laser absorptivity (shown in **Supplementary** Fig. 2) or greater thermal conductivity into the previously fused material. As the laser continues to scan layer 5 of sample S6, we see beads of the melted powder form before a breaking of the surface tension, where the liquid then wets the previous layer. This melt pool behaviour occurs several times over the course of the laser scan, taking place across *ca.* 3.4 ms each time. When the liquid loses its bead shape, the molten material rapidly drops onto the solid material fused in the previous layer while also shifting away from the laser. As such, a continuous melt track is formed, however the frequency of surface waves is greater than that of sample S2 layer 5, albeit with a

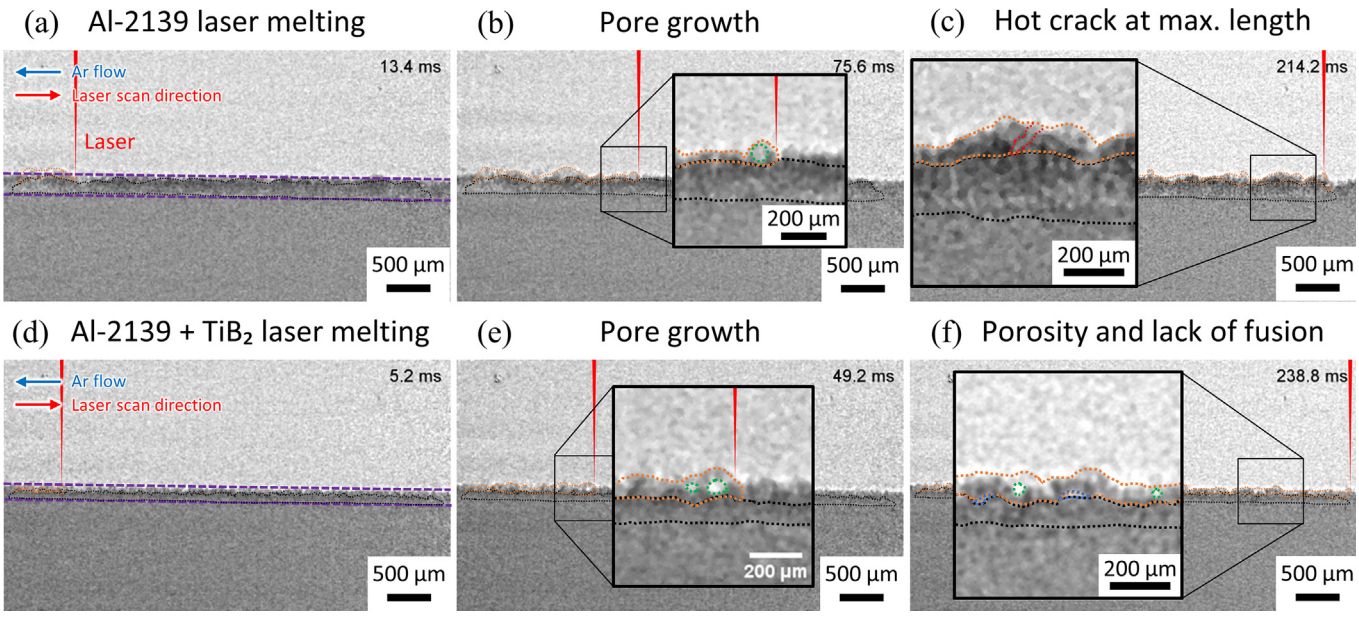

Fig. 2. Time-series radiographs comparing hot cracking during Al-2139 (sample S2 layer 5) and Al-2139 + TiB_2 LPBF (sample S6 layer 5). Insets show a zoom-in of the key features. Direction of the laser beam (red arrow) and gas flow (blue arrow) are shown. (a) Sample S2 melt track prior to layer 5 (black outline) with deposited powder (purple outline) and newly fused material (orange outline). (b) Laser melting in the steady-state region of the melt track, showing a pore (green outline) forming in the molten pool. (c) Laser melting reaches completion, and a hot crack (red outline) develops to its maximum length in the wake of the melt pool. (d) Sample S6 melt track prior to layer 5 (black outline) with deposited powder (white outline) and newly fused material (orange outline). (e) Laser melting in the steady-state region of the melt track, showing two pores (green outline) forming in the molten pool. (f) Laser melting reaches completion. No hot cracks developed, but pores (green outline) and lack of fusion (blue outline) were seen in the finished melt track. (For interpretation of the references to colour in this figure legend, the reader is referred to the web version of this article.)

lower amplitude, as shown in Fig. 2**e**. When wetting of the liquid bead occurs after the breaking of the surface tension, the liquid does not appear to be constrained to the surface of the previous layer in the same way as the liquid solidifying in the wake of a melt pool would be, however further work beyond the scope of this study is needed to verify this observation.

More pores form in the wake of the laser in the grain-refined (GR) build than in the non-GR build. We also see LoF defects in sample S6 layer 5, as shown in Fig. 2**f**. These defects may have formed due to the melt pool behaviour described in the previous paragraph. Once the laser beam moves past the liquid bead and the bead subsequently collapses, there may not be enough residual heat to melt the solid material that it is wetting. Insufficient melting plus thermal contraction of the solidifying material may result in the observed LoF defects.

Hot cracking was not seen *in situ* in the GR builds. The addition of the TiB_2 inoculant promotes a finer columnar solidification front, with shorter, thinner primary dendrite arms of greater number. Although pores can still be encapsulated in this solidification front, the maximum size of pores that can become trapped is reduced as the spacing between dendrites and grains is smaller. Since grain size is reduced by the addition of TiB_2, the length of liquid films at individual grain boundaries in the mushy zone is expected to be shorter. We hypothesis that the smaller grain size reduces the distance a hot crack can propagate through or forces the crack to turn and follow the grain boundaries. In the latter case, growth rate would be reduced as the direction of growth is no longer perpendicular to tensile forces applied by thermal contraction of the cooling material. Cracks instead become more tortuous when propagating through a fine-grained microstructure and have a shorter overall length, which has a reduction on the stress concentration of these features (see evidence in §3.2). The effect of TiB_2 additions on grain boundary angles is also worth considering as cracking in Al alloys generally occurs at the intersection of high angle grain boundaries [59]. The methods used in this study do not capture grain misorientation, but it is of interest to investigate this as future work. Cracks < 100 µm in length, with a width < 15 µm, are not seen in the images due to the spatial resolution limits of the radiography setup. To tackle this, we have carried out high resolution sCT to examine these smaller microstructural features in melt track samples of both materials, which is presented in the following section (§3.2).

From the radiography results, we compare the build quality of Al-2139 + TiB_2 and Al-2139 powders. The layer height built with the grain refined (GR) material is consistently shorter than those built with the non-GR powder under the same processing conditions. For the 20 mm s^{-1} builds, each layer of the GR sample is on average 2.0 µm shorter than those of the non-GR sample, with a standard error of ± 6.5 µm. The difference in height between the two materials increases as the scan speed increases, with the mean height difference being 16 ± 9 µm, 17 ± 6 µm, and 18 ± 6 µm for the 60 mm s^{-1}, 80 mm s^{-1}, and 100 mm s^{-1} builds respectively. For both materials, the overall sample height decreases as scan speed increases. The waviness of the top surface was observed to be greater for the non-GR melt tracks, which is quantified and presented in the following section (§3.3). No other significant differences in the LPBF process for the two materials were observed.

We are confident that the *in situ* observations presented regarding hot cracking and other build features, using the selected process parameters, are relevant to how hot cracks form in high power-high speed LPBF. The cracks we highlight in Fig. 1**f** and Fig. 2**c** form at the end of the melt track, where the laser turns off for those layers. At this location the thermal gradients and cooling rate are greater than in the middle, 'steady-state' region of the melt track [60,61]. Therefore, we see cracks form here that are of a larger size than the cracks that form in the steady-state region. These individual cracks are extreme cases but form due to the same mechanisms as those found in the rest of the samples. Through comparison to a wider range of fully industrially relevant processing parameters [40], and subsequent post-build characterisation, this confirms that the phenomena and underlying mechanisms captured are representative.

3.2. 3D quantification of as-built melt tracks

The use of radiograph images presents challenges when trying to quantify the volume or morphology of microstructural features due to coarse pixel resolution, through thickness integration of the sample, and limited attenuation contrast [21]. Therefore, we performed sCT to better quantify hot cracks and other microstructural features. Fig. 3 shows sCT rendered images of selected samples to highlight the influence of adding TiB_2 across a range of laser scan speeds on the defect distribution in the AM samples. Side views (Fig. 3**c-f**) show where these microstructural features remain in the as-built melt track, with the majority of the larger features lying in the top half of all samples. The location of the defects indicates that the larger cracks were introduced in the final 5 – 7 layers of the build, possibly due to a build-up of residual stress in the latter half of the build driving crack formation, or selective vaporisation of alloying elements due to less thermal conduction from the substrate.

Selective vaporisation of alloying elements reduces the local concentration of certain elements. For alloy susceptibility to hot cracking, the reduction in weight percentage of major alloying elements that form low freezing point phases is most significant. When the local concentration of Cu and Mg is reduced, we can estimate what the effect on the solidification range will be from the respective phase diagrams of these elements with Al. Mg has a lower boiling point that Al and thus we expect the local concentration of Mg to decrease during vaporisation of Al-2139, which would reduce the solidification range. However, Cu has a higher boiling point than Al, and the wt.% Cu in Al-2139 is greater than that of Mg. Therefore, during vaporisation we expect the local concentration of Cu to increase which would increase the solidification range, thus increasing the hot cracking susceptibility of the alloy [40].

The side views of the samples also highlight differences in the surface roughness of the various melt tracks. The Al-2139 samples can be seen to have a greater surface roughness than the Al-2139 + TiB_2 samples on the sides and top due to the presence of partially melted powder particles and molten spatter that has adhered to the track without being consolidated into the melt pool or substantially wetting the solidified material. Reducing v appears to result in fewer partially melted powder particles adhering to the track in the case of both materials.

Fig. 3**g** and **h** show an enlarged view of the microstructural features present in samples S2 and S6, respectively, and illustrates the difference in the size and morphology of both hot cracks and pores between the two materials when processed using the same process parameters. The Al-2139 build contains seven hot cracks in a 300 μm longitudinal section of the track (127 cracks per mm^3 of track), as well as several pores (1070 pores per mm^3 of track) with a volume equivalent diameter (D_{eq}) of the order of 2.7 – 5.8 μm, or 10^1 – 10^2 μm^3.

In a section of the Al-2139 + TiB_2 build of similar size we see fewer hot cracks (116 cracks per mm^3 of track). These hot cracks in the GR sample have a surface area $\sim$ 3.2 times smaller than those in the non-GR sample (1.15 times on average, as shown in Fig. 4**d**), and are more disjointed. This suggests that adding TiB_2 to Al-2139 has mitigated the problem of hot cracking by suppressing crack growth and encouraging the formation of a less detrimental morphology. However, we see a less beneficial result in pore reduction. The pore number in a given volume is similar (1463 pores per mm^3 of track), but the volume of a single pore tends to be greater. This can be seen in inset (h), where two pores present have a D_{eq} on the order of 12.4 – 26.7 μm, or 10^3 – 10^4 μm^3.

The volume fraction of cracks and pores, as well as the total volume fraction, were plotted against *VED* (Fig. 3**i**). The overall trend identified is that the addition of TiB_2 results in a decrease in the volume fraction of cracking at the expense of an increase in the volume fraction of porosity, across all process parameters tested in this study. In 75 % of cases this led to an overall increase in the volume fraction of undesirable microstructural features, reducing part density. Even so, the lowest part density (of sample S6) was still greater than 99.96 %.

For Al-2139, we see from Elambasseril *et al.* [40] that hot cracking can be reduced by increasing *VED* from 20 to *ca.* 2000 J mm^{-3}. However this relationship does not hold true at higher energy densities, since the volume fraction of cracks increases with *VED* from 1667 to 5000 J mm^{-3}, and does not hold true for other aluminium alloys [62–64]. At the lower bound of this *VED* range the total crack volume was calculated to be $\sim$ 12700 μm^3, versus 17300 μm^3 at the upper bound. That being said, *VED* should be used with care as a means of comparison between different AM systems as it is not a universal parameter [65].

When assessing fatigue resistance and mechanical performance related to cracking, metrics other than volume such as crack length, aspect ratio and surface area are generally more relevant. Fig. 4 shows the mean length, breadth, aspect ratio, and surface area of cracks segmented from each sample as a function of *VED*. The crack length, breadth and surface area all increase with increasing *VED* (*i.e.* decreasing scan speed) in the non-GR samples. From 1000 J mm^{-3} to 5000 J mm^{-3}, the crack length increased from 24.0 μm to 27.4 μm, the crack breadth increased from 12.3 μm to 13.3 μm, and the surface area increased from 446.9 μm^2 to 552.9 μm^2. These three changes are related to the dendritic structure. As dendrites tend to become coarser at higher energy densities [40], the liquid channels between dendrites increase in length [31]. This enables larger solidification cracks to form during the final stages of solidification as the liquid in the interdendritic region is torn by interfacial tension from the cooling solid. The mean aspect ratio of cracks in the non-GR samples also increases with increasing *VED*, from 2.26 at the lower bound to 2.38 at the upper bound. Since the grain morphology, and by extension the morphology of liquid channels, does not change significantly with *VED* [40], a minor change in aspect ratio is expected.

In the GR samples the crack length, breadth and surface area are consistent across all process parameters. From 1000 J mm^{-3} to 5000 J mm^{-3} we see a minor decrease of 1.3 μm, 0.6 μm and 47.7 μm^2, respectively. The grain size range is narrower at high energy densities for this material than the non-GR material since significant grain refinement occurs, as seen from 430 J mm^{-3} to 1721 J mm^{-3} [40]. The liquid channels during solidification are therefore shorter and narrower, reducing crack length and breadth.

On the other hand, the aspect ratio of cracks increases with increasing *VED* in the GR samples and is greater on average than that of the non-GR samples. The aspect ratio was calculated as the maximum Feret diameter (*i.e.* length) divided by the maximum distance in a plane orthogonal to maximum Feret diameter (*i.e.* breadth). Given this definition, the increase in aspect ratio with the addition of TiB_2 could be explained by a greater reduction in crack breadth (up to 13.4 %) versus crack length (up to 9.9 %).

Given that pores in the melt pool can influence cracking during solidification, the porosity in the as-built samples was also quantified to reveal overall trends related to the addition of TiB_2 and varying scan speed. Fig. 5 shows the number density of pores (pores per mm^3 of as-built material) plotted against D_{eq}. Across all conditions, pores form that fall within three size ranges. 84 % of pores have a D_{eq} between 2 and 6 μm. 15 % of pores have a D_{eq} between 7 and 20 μm, and the remaining 1 % pores have a D_{eq} $\geq$ 21 μm. Large pores (as seen in Fig. 3**h**) contribute to the overall pore volume more so that the accumulated volume of smaller pores [55], (see Fig. 3**i**).

The melting is believed to have occurred in conduction mode because of the lack of a keyhole in the radiography results, and

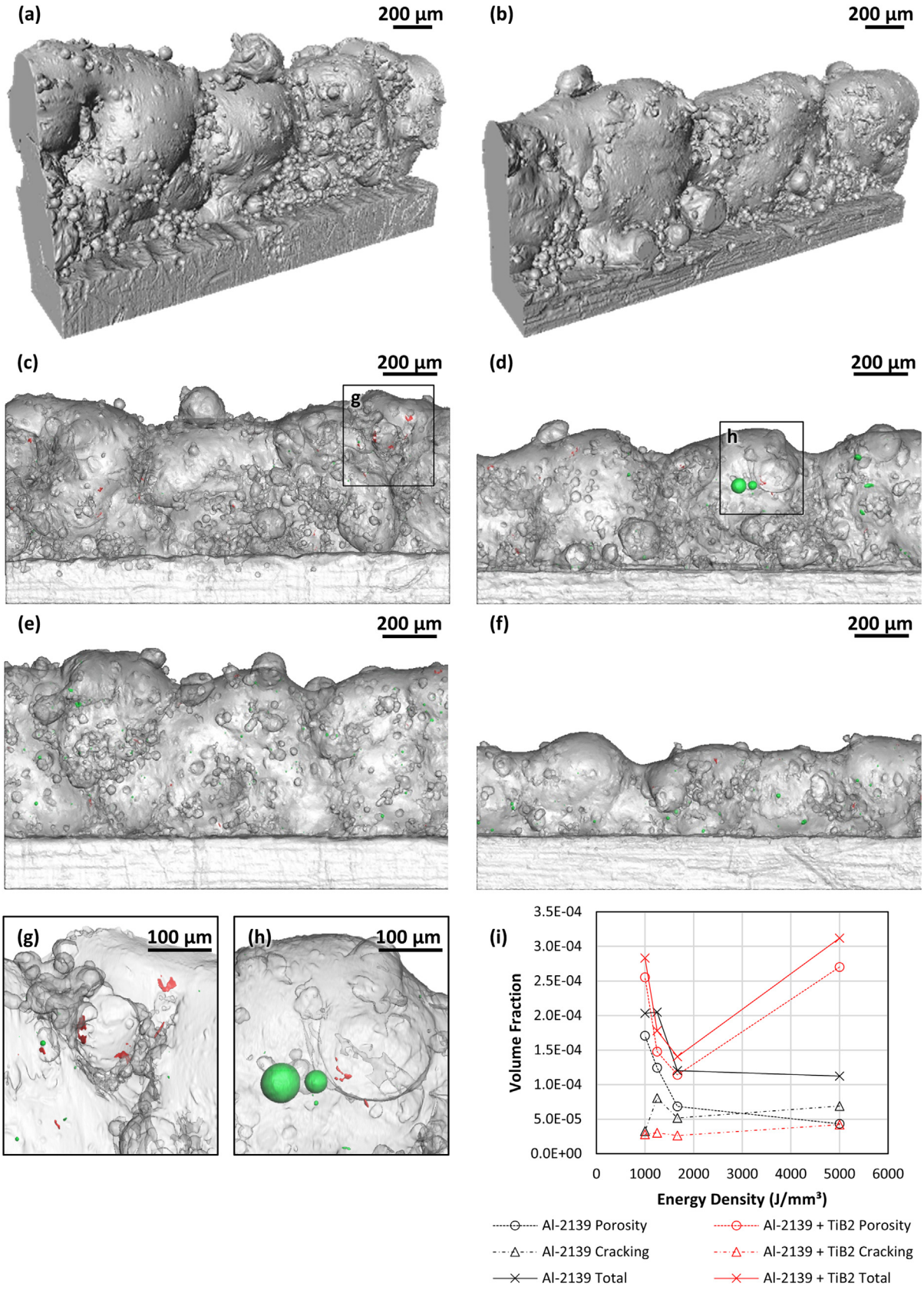

Fig. 3. sCT reconstructions of the LPBF samples. Pores are displayed in green and cracks in red, respectively. a) and b) show a 3D view of the outer surface of samples S2 and S6, respectively. Side views of sample c) S2, d) S6, e) S5, and f) S9 are shown to highlight the difference in build height, surface waviness and powder sintering between the different processing conditions and materials. g) shows small pores and large cracks in sample S2. h) shows large pores and small cracks in sample S6. i) shows a plot of the porosity, cracking, and total volume fraction in each sample. (For interpretation of the references to colour in this figure legend, the reader is referred to the web version of this article.)

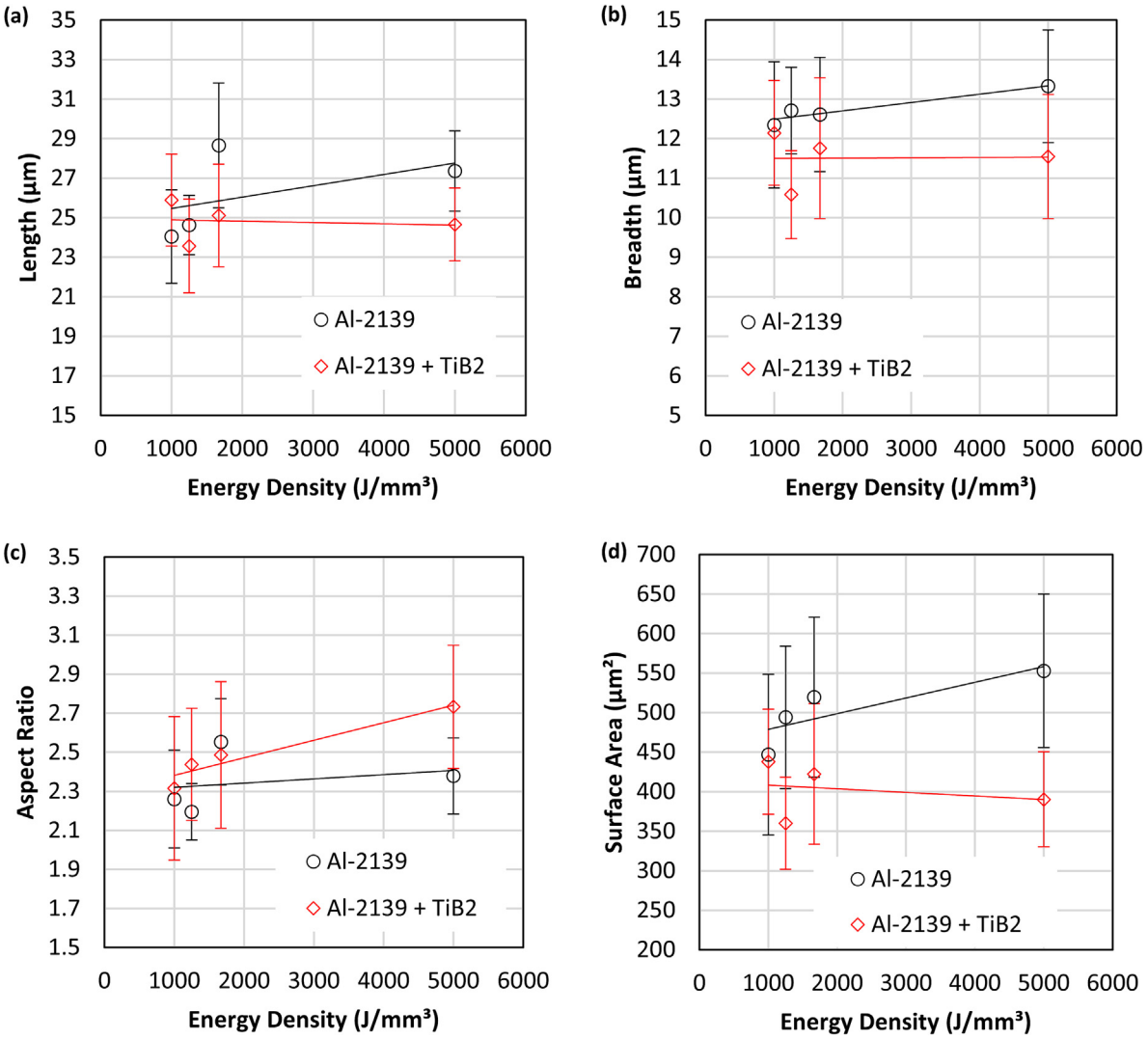

Fig. 4. (a) Mean length, (b) mean breadth, (c) aspect ratio, and (d) surface area of cracks as a function of volume energy density, with error bars showing the standard error.

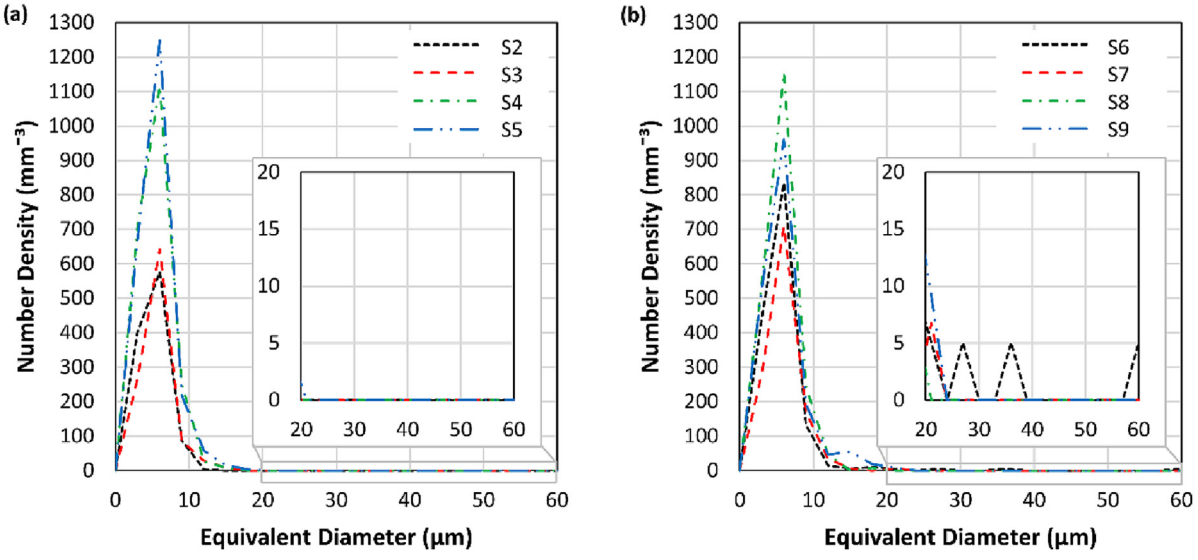

Fig. 5. Number density of pores plotted against equivalent diameter for (a) the Al-2139, and (b) the Al-2139 + TiB_2 samples.

the melt pool depth (shown in **Supplementary** Fig. 5), hence we do not expect keyhole collapse to be a prominent source of porosity. However, keyhole porosity can initiate in transition keyhole regimes [23] so the keyhole collapse mechanism may be responsible for the large pores in low quantities [46,66–68]. Another potential source of porosity is the powder feedstock. For gas-atomised powders, argon gas trapped in powder particles can be entrained into the melt pool during LPBF. Pores can also be introduced via retained soluble gas, which is prevalent in aluminium alloys since hydrogen solubility increases as temperature increases [20]. Hence, we predict powder particle porosity to be the source of the pores with D_{eq} ranging from 7 to 20 μm and retained soluble gas to be the source of the smallest pores in the as-built samples.

When comparing the porosity of the different samples, we see a greater number of pores with D_{eq} ranging from 2 to 20 μm present in the samples produced with a scan speed of 80 mm s^{-1} or greater for both materials. This may be because solidification rates are faster at these speeds which gives pores less time to migrate to the top of the melt pool and escape before being trapped in the solidification front. Although porosity characteristics are broadly similar between the GR and the non-GR samples, there are two notable differences. Firstly, the number of pores in the 2 to 6 μm range is greater in the non-GR sample at the fastest scan speed. Secondly, in the non-GR samples we see no pores with a $D_{eq} \geq 21$ μm. However, in the GR samples these larger pores are present, especially at the slowest scan speed.

3.3. Melt track surface and elemental composition analysis

SEM images of the top and side surfaces of the as-built melt tracks were taken, since X-ray imaging techniques provide limited information regarding surface features. Fractures are visible on the surface of both melt tracks. A minor number of these fractures are cracks that extend into the bulk of the material (see Fig. 6**f**), which are likely to be hot cracks that have propagated to the melt track surface. The majority of the fractures are only present in the oxide layer (Fig. 6**e**), which most likely occur due to the difference in thermal contraction between aluminium and its oxide [3].

Fig. 7 shows various waviness parameters plotted against *VED* for each sample (with the corresponding errors shown in Supplementary Table 4). We calculate that the mean average of deviations (W_a) is greater for the non-GR samples over all processing conditions except when a scan speed of 20 mm s^{-1} is used. The maximum height of irregularities (W_y) was greater in the GR samples in builds with a *VED* < 1600 J mm^{-3}, but this trend reverses at higher *VED*s. When considering the mean vertical distance between the five highest peaks and the five lowest valleys (W_z) we see a similar trend to W_a, with the distance being greater for the non-GR samples, except at the highest *VED*. The root square average of deviations (W_q) also indicates that surface waviness is greater for the non-GR samples when *VED* is < 1600 J mm^{-3}. These results suggest that the addition of TiB_2 can improve the surface finish of LPBF Al-2139 parts but may have a detrimental effect on surface waviness at slower scan speeds. We speculate that these observations may result from the difference in wetting behaviour between the non-GR and GR builds discussed in §3.1, however further work is needed to elucidate the mechanism responsible.

Another feature of the melt tracks identified from the SEM images is a distinct region with lower oxygen content, displayed as a visible difference in greyscale-value in the centre of the top surface. These regions overlap the scan path of the laser, and their width is equal to the laser beam diameter (50 μm, $4\sigma_{x,y}$). EDS of the top surface (**Supplementary** Fig. 6) shows that oxygen concentration is significantly lower on the track surface in this region. Regions of higher oxygen content can be seen either side of these areas. Louvis *et al.* [16] propose that the oxide layer under the laser beam evaporates while remaining on other surfaces. They go on to suggest that Marangoni flow within the melt pool redistributes the oxide of previous build layers when remelting occurs, forming oxide 'walls' adjacent to the laser scan path. In addition, Chia *et al.* [69] show that melt pool flow is responsible for the formation of oxygen-rich streaks regardless of inward or outward Marangoni

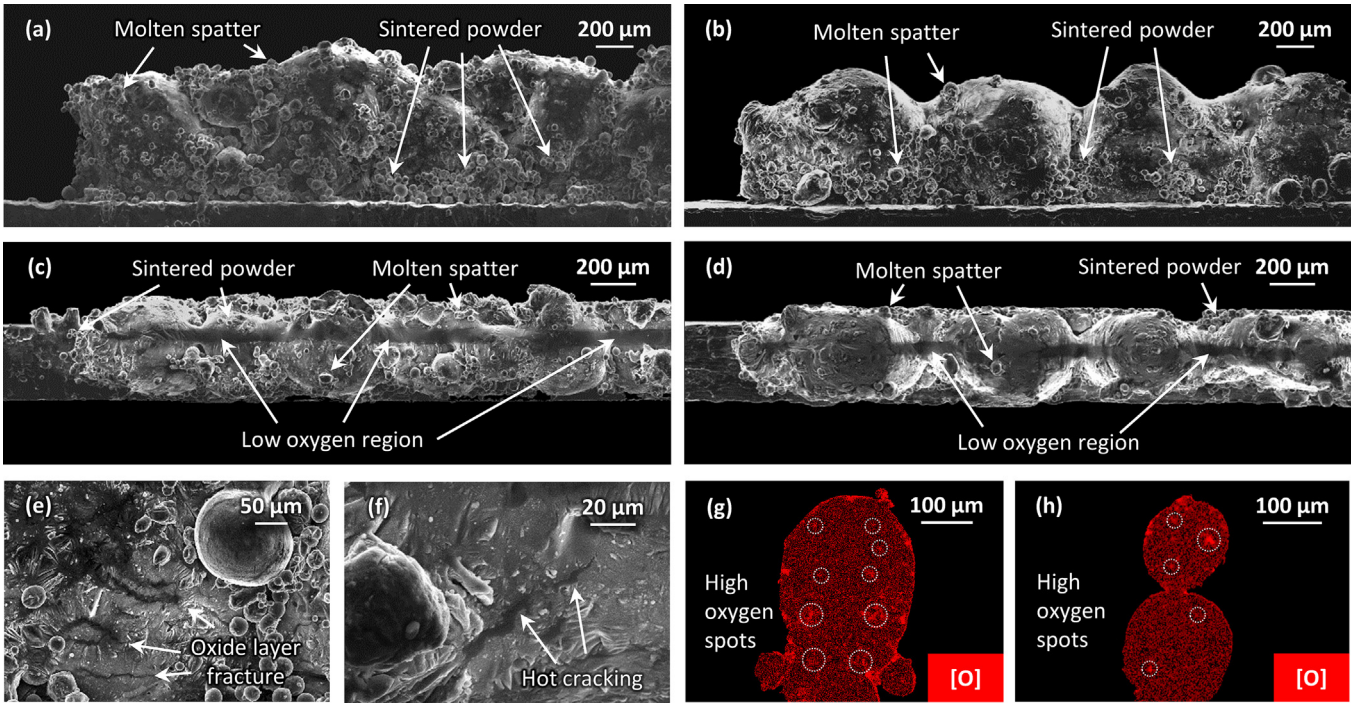

Fig. 6. SEM (secondary electron) images showing top views of (a) sample S2 and (b) S6, as well as side views of (c) S2 and (d) S6 for comparison. The zoomed regions of sample S4 show (e) surface cracks in the oxide layer, and (f) cracks that protrude into the bulk material. EDS oxygen maps of the cross-section of (g) sample S5 and (h) S9. Spots with high oxygen content are highlighted with dotted white circles.

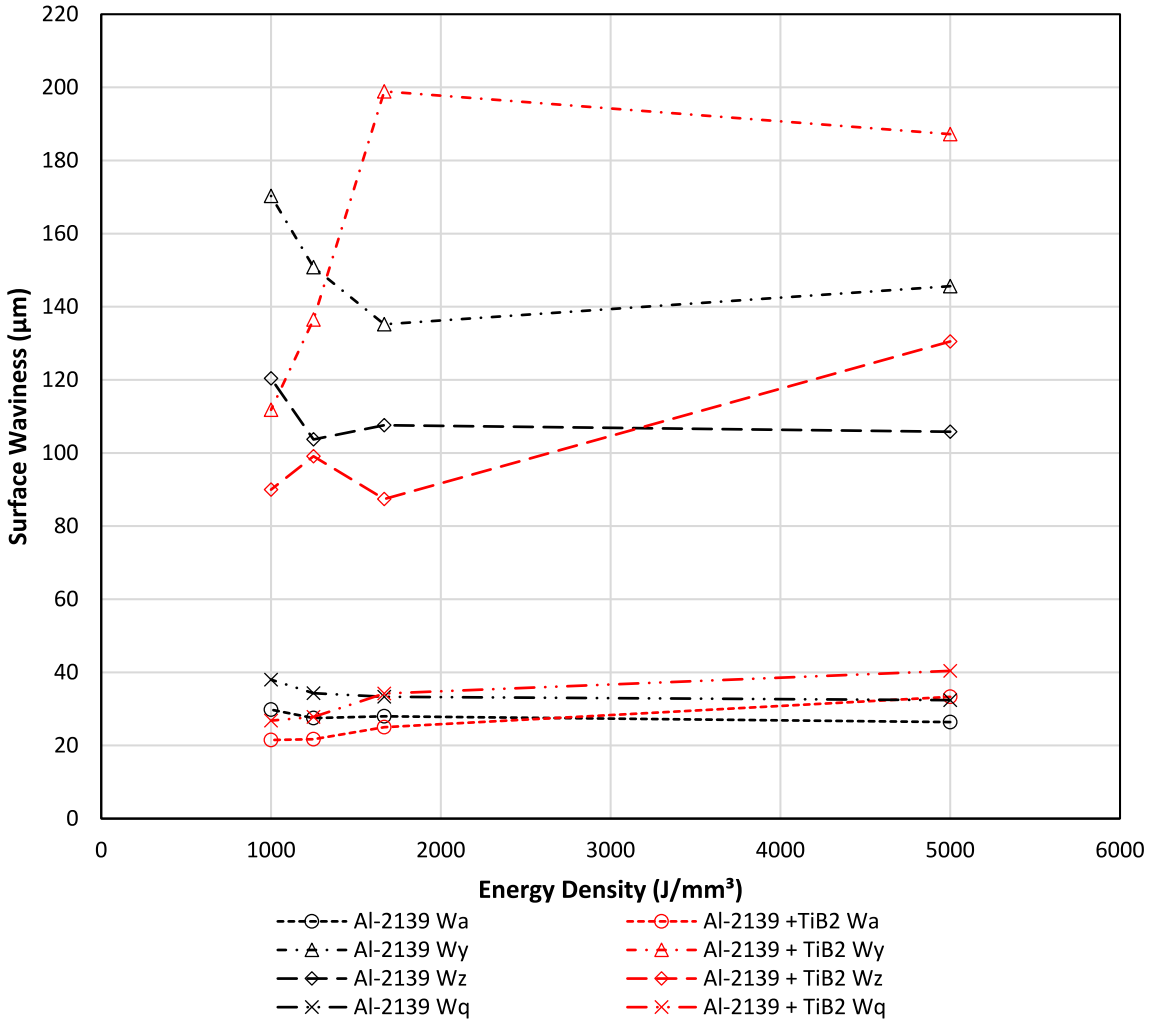

Fig. 7. Surface waviness of the top surface of each sample vs. volume energy density, with surface waviness represented using several parameters (W_a: mean average of deviations, W_y: maximum height of irregularities, W_z: mean vertical distance between the five highest peaks to the five lowest valleys, W_q: root square average of deviations).

Table 2
Elemental composition of the Al-2139 and Al-2139 + TiB_2 melt tracks (surface and cross-section) measured by EDS and normalised.

Sample	Elemental composition (weight %)										
	Al	Cu	Mg	Ag	Mn	V	Fe	Si	Zn	Ti	Cr
Al-2139 alloy specification [72]	91.6 – 94.95	4.5 – 5.5	0.2 – 0.8	0.15 – 0.6	0.2 – 0.6	≤0.05	≤0.15	≤0.10	≤0.25	≤0.15	≤0.05
Al-2139 melt track surface	93.2 ± 0.1	4.2 ± 0.1	1.4 ± 0.1	0.4 ± 0.1	0.4 ± 0.1	0.0 ± 0.1	0.2 ± 0.1	0.1 ± 0.1	0.2 ± 0.1	0.0 ± 0.1	0.0 ± 0.1
Al-2139 + TiB_2 melt track surface	92.6 ± 0.1	5.3 ± 0.1	0.7 ± 0.1	0.4 ± 0.1	0.5 ± 0.1	0.0 ± 0.1	0.1 ± 0.1	0.1 ± 0.1	0.1 ± 0.1	0.2 ± 0.1	0.0 ± 0.1
Al-2139 melt track cross-section	92.9 ± 0.1	5.0 ± 0.1	0.5 ± 0.1	0.2 ± 0.1	0.5 ± 0.1	0.0 ± 0.1	0.1 ± 0.1	0.5 ± 0.1	0.0 ± 0.1	0.0 ± 0.1	0.0 ± 0.1
Al-2139 + TiB_2 melt track cross-section	93.6 ± 0.2	4.6 ± 0.1	0.4 ± 0.1	0.2 ± 0.1	0.4 ± 0.1	0.0 ± 0.1	0.1 ± 0.1	0.3 ± 0.1	0.0 ± 0.1	0.2 ± 0.1	0.0 ± 0.1

flow. They state that when newly melted powder particles saturate the melt pool with oxygen-rich liquid, recoil pressure causes a build-up of this liquid ahead of the laser which subsequently flows to the sides of the melt track. We see spots with high oxygen concentration on the EDS oxygen map of the sample cross-section (Fig. 6**g**) in locations corresponding to the edge of the laser scan path for previous layers, indicating that oxide redistribution has occurred. However, the number of spots does not directly correspond to the number of layers built.

Oxide inclusions can act as nuclei for pore formation [70]. Samuel *et al.* [71] reported that in casting aluminium oxide films trapped in molten metal can lead to the formation of coarse pores and increase the porosity level. In LPBF, Louvis *et al.* [16] report that pores are formed where two oxide films come into contact. Contact of oxide films may explain the presence of the larger pores and some of the intermediate size pores identified in the sCT results ($D_{eq} \geq 21$ µm and 7 to 20 µm, respectively).

EDS has also been used to quantify the weight percentage of each alloying element in the melt tracks. Table 2 shows the elemental composition of the non-GR and GR melt track surface, and cross-section. The weight percentage of Mg is greater at the surface than in the powder or sample cross-section for both materials. This indicates that Mg selectively vaporises before condensing (and solidifying) on the surface of the solidified track,

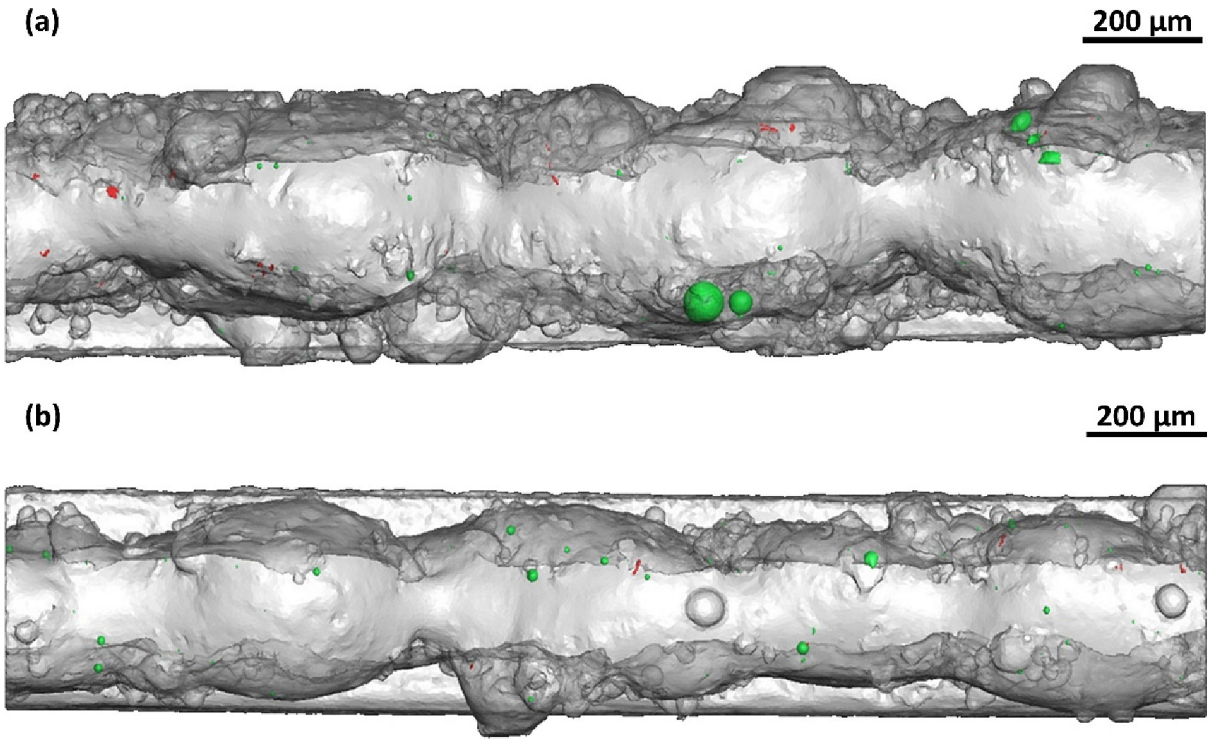

Fig. 8. Sct reconstructions of the lpbf samples. pores are displayed in green and cracks in red, respectively. top views of sample a) s6 and b) s9 are shown to highlight the location of microstructural features in the build plane. (For interpretation of the references to colour in this figure legend, the reader is referred to the web version of this article.)

which matches with prior work in larger LPBF builds [40]. When processing subsequent layers, Mg on remelted surfaces could mix with the newly formed melt pool, resulting in an increase in the local concentration of Mg. Based on the Al-Mg phase diagram, a higher concentration of Mg (up to 18 wt%) increases the solidification range and reduces the solidus temperature, both of which increase the hot cracking susceptibility of the Al-2139 alloy. This may explain why there are more cracks forming near the outer surface of the samples as opposed to the centre of the track (see Fig. 8).

Fig. 8 shows that the majority of the pores are located away from the centre line of the melt track, close to the oxide walls. The redistributed oxide inclusions may act as nuclei for pore formation in LPBF of Al-2139 (with or without TiB_2), similar to those observed in [18].

4. Conclusions

This study investigates the influence of TiB_2 additions and process parameters on hot cracking and melt track formation during multi-layer LPBF of Al-2139 using high speed *in situ* synchrotron radiography coupled with synchrotron X-ray computed tomography, SEM imaging and EDS analysis of the as-built samples. From our results we draw the following conclusions:

1. The evolution of hot cracking was observed in Al-2139, capturing cracks of 106 – 110 µm in length forming at the end of the melt track, after lasing was completed. Crack growth took place over 1.0 – 1.4 ms at a rate of 76 – 110 mm s^{-1}.
2. The addition of TiB_2 reduces the volume fraction of hot cracks across all process parameters tested in this study. The greatest difference between the grain refined and the non-grain refined material was a reduction in volume fraction of 79 % in samples built with a *VED* of 1250 J mm^{-3}, and the smallest difference was a reduction of 52 % in samples built with a *VED* of 5000 J mm^{-3}.
3. The average length, breadth, and surface area of cracks is reduced by adding TiB_2, indicating that TiB_2 also reduces the stress concentration effect of individual defects in Al-2139 parts.
4. The drawback of adding TiB_2 to Al-2139 is an increase in the pore volume. The reason is unclear, and the result does not fit with observations in casting. Powder particle porosity and retained soluble gas porosity was present in all samples but larger pores were only seen in the grain refined material. Although the larger pores were in low number, they have a substantial effect on part density.

Data availability

Data will be made available on request.

Declaration of Competing Interest

The authors declare that they have no known competing financial interests or personal relationships that could have appeared to influence the work reported in this paper.

Acknowledgements

The authors acknowledge financial support from the EPSRC MAPP Future Manufacturing Hub (EP/P006566/1, www.mapp.ac.uk); The Royal Academy of Engineering (CiET1819/10);); UK-EPSRC (grants EP/W031167/1, EP/W032147/1, EP/W037483/1, EP/W006774/1, EP/W003333/1, EP/V061798/1); Rolls-Royce Plc. through the Horizon 2020 Clean Sky 2 WP5.8.1 programmes and DTR's Industrial Case studentship. We acknowledge the Research Complex at Harwell for use of the facilities and thank Diamond Light Source Ltd. (DLS) for providing beamtime (MT19354-1 and CM22976-3) at the I13-2 Diamond Manchester Imaging Branchline. Special thanks to Philip Holloway (Photron Ltd.) for providing

the high-speed camera (FASTCAM SAZ 2100K) to perform this experiment.

Author contributions

CLAL, PDL, ME and DTR conceived of the project. MB and JE undertook the initial investigations on LPBF of Al-2139 from which this project was instigated. DTR and CLAL designed and performed the experiments, with all authors contributing. DTR performed sCT, SEM, data analysis, and results interpretation. DTR, CLAL, and PDL led the results interpretation and paper writing.

Appendix A. Supplementary data

Supplementary data to this article can be found online at https://doi.org/10.1016/j.matdes.2023.112031.

References

[1] S. Sun, M. Brandt, M. Easton, in: Powder bed fusion processes: An overview, Elsevier Ltd, 2017, https://doi.org/10.1016/B978-0-08-100433-3.00002-6.
[2] T.M. Pollock, Alloy design for aircraft engines, Nat. Mater. 15 (2016) 809–815, https://doi.org/10.1038/nmat4709.
[3] E.O. Olakanmi, R.F. Cochrane, K.W. Dalgarno, A review on selective laser sintering/melting (SLS/SLM) of aluminium alloy powders: Processing, microstructure, and properties, Prog. Mater. Sci. 74 (2015) 401–477, https://doi.org/10.1016/j.pmatsci.2015.03.002.
[4] C.A. Brice, W.A. Tayon, J.A. Newman, M.V. Kral, C. Bishop, A. Sokolova, Effect of compositional changes on microstructure in additively manufactured aluminum alloy 2139, Mater. Charact. 143 (2018) 50–58, https://doi.org/10.1016/j.matchar.2018.04.002.
[5] N.T. Aboulkhair, M. Simonelli, L. Parry, I. Ashcroft, C. Tuck, R. Hague, 3D printing of Aluminium alloys: Additive Manufacturing of Aluminium alloys using selective laser melting, Prog. Mater Sci. 106 (2019), https://doi.org/10.1016/j.pmatsci.2019.100578 100578.
[6] Y.N. Hu, S.C. Wu, P.J. Withers, J. Zhang, H.Y.X. Bao, Y.N. Fu, G.Z. Kang, The effect of manufacturing defects on the fatigue life of selective laser melted Ti-6Al-4V structures, Mater. Des. 192 (2020), https://doi.org/10.1016/j.matdes.2020.108708.
[7] A. du Plessis, I. Yadroitsava, I. Yadroitsev, Effects of defects on mechanical properties in metal additive manufacturing: A review focusing on X-ray tomography insights, Mater. Des. 187 (2020), https://doi.org/10.1016/j.matdes.2019.108385 108385.
[8] A. Cho, W.B. Lisagor, T.T. Bales, Development and Processing Improvement of Aerospace Aluminum Alloys - Development of Al-Cu-Mg-Ag Alloy (2139), 2007.
[9] W.E. Frazier, Metal Additive Manufacturing: A Review, J. Mater. Eng. Perform. 23 (2014) 1917–1928, https://doi.org/10.1007/s11665-014-0958-z.
[10] B. Wysocki, P. Maj, R. Sitek, J. Buhagiar, K.J. Kurzydłowski, W. Świeszkowski, Laser and electron beam additive manufacturing methods of fabricating titanium bone implants, Applied Sciences (Switzerland). 7 (2017) 1–20, https://doi.org/10.3390/app7070657.
[11] L. Bolzoni, M. Xia, N.H. Babu, Formation of equiaxed crystal structures in directionally solidified Al-Si alloys using Nb-based heterogeneous nuclei, Sci. Rep. 6 (2016) 1–10, https://doi.org/10.1038/srep39554.
[12] J.H. Martin, B.D. Yahata, J.M. Hundley, J.A. Mayer, T.A. Schaedler, T.M. Pollock, 3D printing of high-strength aluminium alloys, Nature 549 (2017) 365–369, https://doi.org/10.1038/nature23894.
[13] J.P. Kruth, L. Froyen, J. Van Vaerenbergh, P. Mercelis, M. Rombouts, B. Lauwers, Selective laser melting of iron-based powder, J. Mater. Process. Technol. 149 (2004) 616–622, https://doi.org/10.1016/j.jmatprotec.2003.11.051.
[14] D. Greitemeier, F. Palm, F. Syassen, T. Melz, Fatigue performance of additive manufactured TiAl6V4 using electron and laser beam melting, Int. J. Fatigue 94 (2017) 211–217, https://doi.org/10.1016/j.ijfatigue.2016.05.001.
[15] R. Snell, S. Tammas-Williams, L. Chechik, A. Lyle, E. Hernández-Nava, C. Boig, G. Panoutsos, I. Todd, Methods for Rapid Pore Classification in Metal Additive Manufacturing, JOM 72 (2020) 101–109, https://doi.org/10.1007/s11837-019-03761-9.
[16] E. Louvis, P. Fox, C.J. Sutcliffe, Selective laser melting of aluminium components, J. Mater. Process. Technol. 211 (2011) 275–284, https://doi.org/10.1016/j.jmatprotec.2010.09.019.
[17] M.N. Ahsan, R. Bradley, A.J. Pinkerton, Microcomputed tomography analysis of intralayer porosity generation in laser direct metal deposition and its causes, J. Laser Appl. 23 (2011), https://doi.org/10.2351/1.3582311 022009.
[18] C.L.A. Leung, S. Marussi, M. Towrie, R.C. Atwood, P.J. Withers, P.D. Lee, The effect of powder oxidation on defect formation in laser additive manufacturing, Acta Mater. 166 (2019) 294–305, https://doi.org/10.1016/j.actamat.2018.12.027.
[19] C. Iantaffi, C. Lun, A. Leung, Y. Chen, S. Guan, R.C. Atwood, J. Lertthanasarn, M. Pham, M. Meisnar, T. Rohr, P.D. Lee, Oxidation induced mechanisms during directed energy deposition additive manufactured titanium alloy builds, Additive Manufacturing Letters. 1 (2021), https://doi.org/10.1016/j.addlet.2021.100022 100022.
[20] P.D. Lee, J.D. Hunt, Measuring the nucleation of hydrogen porosity during the solidification of aluminium-copper alloys, Scr. Mater. 36 (1997) 399–404, https://doi.org/10.1016/S1359-6462(96)00411-3.
[21] C.L.A. Leung, S. Marussi, M. Towrie, V. Garcia, R.C. Atwood, A.J. Bodey, J.R. Jones, P.J. Withers, P.D. Lee, Laser-matter interactions in additive manufacturing of stainless steel SS316L and 13–93 bioactive glass revealed by in situ X-ray imaging, Addit. Manuf. 24 (2018) 647–657, https://doi.org/10.1016/j.addma.2018.08.025.
[22] C.L.A. Leung, I. Elizarova, M. Isaacs, S. Marathe, E. Saiz, P.D. Lee, Enhanced near-infrared absorption for laser powder bed fusion using reduced graphene oxide, Appl. Mater. Today 23 (2021), https://doi.org/10.1016/j.apmt.2021.101009 101009.
[23] Y. Huang, T.G. Fleming, S.J. Clark, S. Marussi, K. Fezzaa, J. Thiyagalingam, C.L.A. Leung, P.D. Lee, Keyhole fluctuation and pore formation mechanisms during laser powder bed fusion additive manufacturing, Nat. Commun. 13 (2022) 1–11, https://doi.org/10.1038/s41467-022-28694-x.
[24] L.N. Carter, M.M. Attallah, R.C. Reed, Laser powder bed fabrication of nickel-base superalloys: Influence of parameters; characterisation, quantification and mitigation of cracking, Proceedings of the International Symposium on Superalloys. (2012) 577–586. https://doi.org/10.7449/2012/superalloys_2012_577_586.
[25] A. Aversa, G. Marchese, A. Saboori, E. Bassini, D. Manfredi, G. Marchese, A. Saboori, E. Bassini, P. Fino, M. Lombardi, D. Manfredi, S. Biamino, D. Ugues, P. Fino, New Aluminum Alloys Specifically Designed for Laser Powder Bed Fusion : A Review (2019), https://doi.org/10.3390/ma12071007.
[26] J. Liu, S. Kou, Susceptibility of ternary aluminum alloys to cracking during solidification, Acta Mater. 125 (2017) 513–523, https://doi.org/10.1016/j.actamat.2016.12.028.
[27] X. Zhang, H. Chen, L. Xu, J. Xu, X. Ren, X. Chen, Cracking mechanism and susceptibility of laser melting deposited Inconel 738 superalloy, Mater. Des. 183 (2019), https://doi.org/10.1016/j.matdes.2019.108105 108105.
[28] C. Qiu, H. Chen, Q. Liu, S. Yue, H. Wang, On the solidification behaviour and cracking origin of a nickel-based superalloy during selective laser melting, Mater Charact 148 (2019) 330–344, https://doi.org/10.1016/j.matchar.2018.12.032.
[29] M. Saadati, A.K. Edalat Nobarzad, M. Jahazi, On the hot cracking of HSLA steel welds: Role of epitaxial growth and HAZ grain size, J. Manuf. Process. 41 (2019) 242–251, https://doi.org/10.1016/j.jmapro.2019.03.032.
[30] M. Rappaz, J. Drezet, M. Gremaud, A New Hot-Tearing Criterion 30 (1999) 449–455.
[31] A.B. Phillion, R.W. Hamilton, D. Fuloria, A.C.L. Leung, P. Rockett, T. Connolley, P. D. Lee, In situ X-ray observation of semi-solid deformation and failure in Al-Cu alloys, Acta Mater. 59 (2011) 1436–1444, https://doi.org/10.1016/j.actamat.2010.11.005.
[32] G. Mathers, Welding metallurgy, in: The Welding of Aluminium and Its Alloys, Elsevier, 2002: pp. 10–34. https://doi.org/10.1533/9781855737631.10.
[33] S. Katayama, Defect formation mechanisms and preventive procedures in laser welding, in: Handbook of Laser Welding Technologies, Elsevier, n.d.: pp. 332–373. https://doi.org/10.1533/9780857098771.2.332.
[34] N.E. Hodge, R.M. Ferencz, J.M. Solberg, Implementation of a thermomechanical model for the simulation of selective laser melting, Comput. Mech. 54 (2014) 33–51, https://doi.org/10.1007/s00466-014-1024-2.
[35] Y. Kok, X.P. Tan, P. Wang, M.L.S. Nai, N.H. Loh, E. Liu, S.B. Tor, Anisotropy and heterogeneity of microstructure and mechanical properties in metal additive manufacturing: A critical review, Mater. Des. 139 (2018) 565–586, https://doi.org/10.1016/j.matdes.2017.11.021.
[36] G. Agarwal, M. Amirthalingam, S.C. Moon, R.J. Dippenaar, I.M. Richardson, M.J. M. Hermans, Experimental evidence of liquid feeding during solidification of a steel, Scr. Mater. 146 (2018) 105–109, https://doi.org/10.1016/j.scriptamat.2017.11.003.
[37] W. Stopyra, K. Gruber, I. Smolina, T. Kurzynowski, B. Kuźnicka, Laser powder bed fusion of AA7075 alloy: Influence of process parameters on porosity and hot cracking, Addit. Manuf. 35 (2020), https://doi.org/10.1016/j.addma.2020.101270.
[38] M. Easton, D. Stjohn, Grain refinement of aluminum alloys: Part I. The nucleant and solute paradigms - a review of the literature, Metall. Mater. Trans. A Phys. Metall. Mater. Sci. 30 (1999) 1613–1623, https://doi.org/10.1007/s11661-999-0098-5.
[39] I.T. Ho, Y.T. Chen, A.C. Yeh, C.P. Chen, K.K. Jen, Microstructure evolution induced by inoculants during the selective laser melting of IN718, Addit. Manuf. 21 (2018) 465–471, https://doi.org/10.1016/j.addma.2018.02.018.
[40] J. Elambasseril, M.J. Benoit, S. Zhu, M.A. Easton, E. Lui, C.A. Brice, M. Qian, M. Brandt, Effect of process parameters and grain refinement on hot tearing susceptibility of high strength aluminum alloy 2139 in laser powder bed fusion, Progress in Additive Manufacturing. (2022), https://doi.org/10.1007/s40964-021-00259-2.
[41] X. Wang, K. Chou, EBSD study of beam speed effects on Ti-6Al-4V alloy by powder bed electron beam additive manufacturing, J. Alloy. Compd. 748 (2018) 236–244, https://doi.org/10.1016/j.jallcom.2018.03.173.

[42] H.L. Wei, J. Mazumder, T. DebRoy, Evolution of solidification texture during additive manufacturing, Sci. Rep. 5 (2015) 1–7, https://doi.org/10.1038/srep16446.
[43] L. Thijs, K. Kempen, J. Kruth, J. Van Humbeeck, Fine-structured aluminium products with controllable texture by selective laser melting of pre-alloyed AlSi10Mg powder, Acta Mater. 61 (2013) 1809–1819, https://doi.org/10.1016/j.actamat.2012.11.052.
[44] P.-J. Chiang, R. Jiang, R. Cunningham, N. Parab, C. Zhao, K. Fezzaa, T. Sun, A.D. Rollett, In Situ Characterization of Hot Cracking Using Dynamic X-Ray Radiography, Advanced Real Time Imaging II (2019) 77–85, https://doi.org/10.1007/978-3-030-06143-2_8.
[45] H. Ghasemi-tabasi, C. De Formanoir, S. Van Petegem, J. Jhabvala, S. Hocine, E. Boillat, N. Sohrabi, F. Marone, D. Grolimund, H. Van Swygenhoven, R.E. Log, Direct observation of crack formation mechanisms with operando Laser Powder Bed Fusion X-ray imaging, 51 (2022) 0–10. https://doi.org/10.1016/j.addma.2022.102619.
[46] C.L.A. Leung, S. Marussi, R.C. Atwood, M. Towrie, P.J. Withers, P.D. Lee, In situ X-ray imaging of defect and molten pool dynamics in laser additive manufacturing, Nat. Commun. 9 (2018) 1–9, https://doi.org/10.1038/s41467-018-03734-7.
[47] N. Nadammal, T. Mishurova, T. Fritsch, I. Serrano-Munoz, A. Kromm, C. Haberland, P.D. Portella, G. Bruno, Critical role of scan strategies on the development of microstructure, texture, and residual stresses during laser powder bed fusion additive manufacturing, Addit. Manuf. 38 (2021), https://doi.org/10.1016/j.addma.2020.101792 101792.
[48] R. Indhu, V. Vivek, L. Sarathkumar, A. Bharatish, S. Soundarapandian, Overview of Laser Absorptivity Measurement Techniques for Material Processing, (2018) 458–481.
[49] T. Kurzynowski, W. Stopyra, K. Gruber, G. Ziólkowski, B. Kuznicka, E. Chlebus, Effect of scanning and support strategies on relative density of SLM-ed H13 steel in relation to specimen size, Materials. 12 (2019), https://doi.org/10.3390/ma12020239.
[50] C. Rau, U. Wagner, Z. Pešić, A. De Fanis, Coherent imaging at the Diamond beamline I13, Physica Status Solidi (A) Applications and Materials Science. 208 (2011) 2522–2525. https://doi.org/10.1002/pssa.201184272.
[51] N. Wadeson, M. Basham, Savu: A Python-based, MPI Framework for Simultaneous Processing of Multiple, N-dimensional, Large Tomography Datasets, ArXiv. abs/1610.0 (2016).
[52] S. Preibisch, S. Saalfeld, P. Tomancak, Globally optimal stitching of tiled 3D microscopic image acquisitions, Bioinformatics 25 (2009) 1463–1465, https://doi.org/10.1093/bioinformatics/btp184.
[53] K. Dabov, A. Foi, V. Katkovnik, K. Egiazarian, Image Denoising by Sparse 3-D Transform-Domain Collaborative Filtering, IEEE Trans. Image Process. 16 (2007) 2080–2095, https://doi.org/10.1109/TIP.2007.901238.
[54] C.L.A. Leung, R. Tosi, E. Muzangaza, S. Nonni, P.J. Withers, P.D. Lee, Effect of preheating on the thermal, microstructural and mechanical properties of selective electron beam melted Ti-6Al-4V components, Mater. Des. 174 (2019), https://doi.org/10.1016/j.matdes.2019.107792 107792.
[55] L. Sinclair, C.L.A. Leung, S. Marussi, S.J. Clark, Y. Chen, M.P. Olbinado, A. Rack, J. Gardy, G.J. Baxter, P.D. Lee, In situ radiographic and ex situ tomographic analysis of pore interactions during multilayer builds in laser powder bed fusion, Addit. Manuf. 36 (2020), https://doi.org/10.1016/j.addma.2020.101512.
[56] S. Ly, A.M. Rubenchik, S.A. Khairallah, G. Guss, J. Manyalibo, Metal vapor micro-jet controls material redistribution in laser powder bed fusion additive manufacturing, (2017) 1–12. https://doi.org/10.1038/s41598-017-04237-z.
[57] S.A. Khairallah, A.T. Anderson, A. Rubenchik, W.E. King, Laser powder-bed fusion additive manufacturing: Physics of complex melt flow and formation mechanisms of pores, spatter, and denudation zones, Acta Mater. 108 (2016) 36–45, https://doi.org/10.1016/j.actamat.2016.02.014.
[58] L. Aucott, H. Dong, W. Mirihanage, R. Atwood, A. Kidess, S. Gao, S. Wen, J. Marsden, S. Feng, M. Tong, T. Connolley, M. Drakopoulos, C.R. Kleijn, I.M. Richardson, D.J. Browne, R.H. Mathiesen, H.V. Atkinson, Revealing internal flow behaviour in arc welding and additive manufacturing of metals, Nat. Commun. 9 (2018) 1–7, https://doi.org/10.1038/s41467-018-07900-9.
[59] A. Sonawane, G. Roux, J. Blandin, A. Despres, G. Martin, Materialia Cracking mechanism and its sensitivity to processing conditions during laser powder bed fusion of a structural aluminum alloy, Materialia (Oxf). 15 (2021), https://doi.org/10.1016/j.mtla.2020.100976 100976.
[60] T. DebRoy, H.L. Wei, J.S. Zuback, T. Mukherjee, J.W. Elmer, J.O. Milewski, A.M. Beese, A. Wilson-Heid, A. De, W. Zhang, Additive manufacturing of metallic components – Process, structure and properties, Prog. Mater Sci. 92 (2018) 112–224, https://doi.org/10.1016/j.pmatsci.2017.10.001.
[61] P.A. Hooper, Melt pool temperature and cooling rates in laser powder bed fusion, Addit. Manuf. 22 (2018) 548–559, https://doi.org/10.1016/j.addma.2018.05.032.
[62] H. Hyer, L. Zhou, A. Mehta, S. Park, T. Huynh, S. Song, Y. Bai, K. Cho, B. McWilliams, Y. Sohn, Composition-dependent solidification cracking of aluminum-silicon alloys during laser powder bed fusion, Acta Mater. 208 (2021), https://doi.org/10.1016/j.actamat.2021.116698 116698.
[63] A. Mehta, L. Zhou, T. Huynh, S. Park, H. Hyer, S. Song, Y. Bai, D.D. Imholte, N.E. Woolstenhulme, D.M. Wachs, Y. Sohn, Additive manufacturing and mechanical properties of the dense and crack free Zr-modified aluminum alloy 6061 fabricated by the laser-powder bed fusion, Addit. Manuf. 41 (2021), https://doi.org/10.1016/j.addma.2021.101966 101966.
[64] L. Zhou, H. Hyer, J. Chang, A. Mehta, T. Huynh, Y. Yang, Y. Sohn, Microstructure, mechanical performance, and corrosion behavior of additively manufactured aluminum alloy 5083 with 0.7 and 1.0 wt% Zr addition, Mater. Sci. Eng. A 823 (2021), https://doi.org/10.1016/j.msea.2021.141679 141679.
[65] B. Rankouhi, A.K. Agrawal, F.E. Pfefferkorn, D.J. Thoma, A dimensionless number for predicting universal processing parameter boundaries in metal powder bed additive manufacturing, Manuf Lett. 27 (2021) 13–17, https://doi.org/10.1016/j.mfglet.2020.12.002.
[66] C. Zhao, N.D. Parab, X. Li, K. Fezzaa, W. Tan, A.D. Rollett, T. Sun, Critical instability at moving keyhole tip generates porosity in laser melting, Science 370 (2020) (1979) 1080–1086, https://doi.org/10.1126/science.abd1587.
[67] C.L.A. Leung, D. Luczyniec, E. Guo, S. Marussi, R.C. Atwood, M. Meisnar, B. Saunders, P.D. Lee, Quantification of Interdependent Dynamics during Laser Additive Manufacturing Using X-Ray Imaging Informed Multi-Physics and Multiphase Simulation, Adv. Sci. 9 (2022) 2203546, https://doi.org/10.1002/advs.202203546.
[68] A.A. Martin, N.P. Calta, S.A. Khairallah, J. Wang, P.J. Depond, A.Y. Fong, V. Thampy, G.M. Guss, A.M. Kiss, K.H. Stone, C.J. Tassone, J. Nelson Weker, M.F. Toney, T. van Buuren, M.J. Matthews, Dynamics of pore formation during laser powder bed fusion additive manufacturing, Nat Commun. 10 (2019) 1987. https://doi.org/10.1038/s41467-019-10009-2.
[69] H.Y. Chia, L. Wang, W. Yan, Influence of oxygen content on melt pool dynamics in metal additive manufacturing: High-fidelity modeling with experimental validation, Acta Mater. 249 (2023), https://doi.org/10.1016/j.actamat.2023.118824 118824.
[70] P.D. Lee, S. Sridhar, Direct observation of the effect of strontium on porosity formation during the solidification of aluminium-silicon alloys, Int. J. Cast Met. Res. 13 (2000) 185–198, https://doi.org/10.1080/13640461.2000.11819401.
[71] A.M. Samuel, F.H. Samuel, H.W. Doty, S. Valtierra, Influence of oxides on porosity formation in Sr-treated alloys, Int. J. Met. 11 (2017) 729–742, https://doi.org/10.1007/s40962-016-0118-3.
[72] The Aluminium Association, International Alloy Designations and Chemical Composition Limits for Wrought Aluminum and Wrought Aluminum Alloys With Support for On-line Access From: Aluminum Extruders Council Use of the Information, The Aluminum Association, Arlington, Virginia. (2015) 31. https://www.aluminum.org/sites/default/files/Teal Sheets.pdf (accessed March 11, 2020).